Current Distribution in PEM Fuel Cells. Part 1: Oxygen and Fuel Flow Rate Effects

Dilip Natarajan and Trung Van Nguyen
Dept. of Chemical and Petroleum Engineering, University of Kansas, Lawrence, KS 66045

DOI 10.1002/aic.10545
Published online June 27, 2005 in Wiley InterScience (www.interscience.wiley.com).

A segmented electrode/current collector setup was used to examine the effect of oxygen flow rate, anode sparger temperature, and hydrogen starvation on the spatial and temporal distribution of local current densities along a single gas channel in a PEM fuel cell operated on pure hydrogen and oxygen. Uniformity in local current densities at a given voltage was sustained over longer periods of time with higher oxygen flow rates that enhanced liquid water removal. When water removal rate was not sufficient, electrode flooding occurred in segments that were farthest from the gas inlet. Increasing anode sparger temperature resulted in reduction of water removal rate from the cathode by back diffusion leading to performance reduction of downstream segments. When fuel was in excess, the current density distribution was dominated by the hydration pattern of the membrane electrode assembly. When fuel supply was less than the electrochemical reaction demand, segments furthest from the inlet suffered fuel starvation, resulting in loss of performance. The use of one of the electrode segments as a novel in-line voltage sensor to reflect available reactant concentrations was also demonstrated. Air operation and effect of cell temperature were also examined and the results are presented in the second part of this series. © 2005 American Institute of Chemical Engineers *AIChE J,* 51: 2587–2598, 2005

Keywords: PEM fuel cells, conventional gas distributor, current density distribution, segmented electrode, hydrogen starvation

Introduction

Features such as high energy efficiency, simplicity in design, and operational and environmental benefits offered by proton-exchange-membrane (PEM) fuel cells make them a promising candidate for future energy conversion needs, leading to an exponential increase in global research in this area over the past two decades. The research effort has been primarily directed toward a fundamental understanding and alleviation of the efficiency-limiting phenomena occurring in the PEM fuel cell system to make them commercially viable and cost competitive with current energy-conversion devices. The performance-limiting characteristics in PEM fuel cells can be broadly classified into activation losses, ohmic potential drop, and mass-transfer limitations that are directly related to the distribution of catalyst, reactants, product, and ohmic resistances over the reactive area. The distribution of the above-mentioned parameters determines the local current density distribution and thus the average current density and performance at any given operating voltage.

Given the difficulties associated with the direct measurement of species concentration, catalyst activity, and the like, stemming from the small dimensional scales and extreme aspect ratios associated with the fuel cell components, researchers in the past resorted to elaborate mathematical models to map the distribution of the relevant parameters.[1-11] However, experimental data on local current density distribution are essential to validate these models and to transform them into predictive tools that can assist the fuel cell design process. This need for spatial (and temporal) current distribution information and the advancement in segmented fuel cell fabrication techniques

Correspondence concerning this article should be addressed to T. V. Nguyen at cptvn@ku.edu.

have resulted in a number of publications in the recent past addressing local current density measurements.

Cleghorn et al.[12] conducted the first current density distribution measurements on typical lab-scale PEM fuel cell setups using printed circuit board (PCB) technology to create a segmented current collector and multichannel flow field. Stumper et al.[13] analyzed three methods for current density distribution mapping. The methods suggested by Stumper and coworkers were: (1) the partial membrane electrode assembly (MEA) approach involving the use of several different MEAs with a catalyzed active area of varying fractions of the total flow field area; (2) the subcell technique where a number of "subcells" are placed at various locations along the gas flow channel that were electrically insulated from the main active MEA; and (3) the current-mapping technique, where a network of passive graphite resistors were placed between the flow-field plate and the current-collecting bus plate, and the potential drop across these resistors was monitored to establish the current flowing through them. Wieser et al.[14] proposed the use of an array of Hall sensors with a segmented current collector and flow field for local current density measurements. Most of the aforementioned techniques were plagued by complications arising from the use of a single potentiostat/multiplexer combination to control the individual segments, loss in resolution attributed to current spreading within the unsegmented electrode (or bus plate in the case of the third approach by Stumper et al.[13]), and/or current-collector segmentation being applied to only one side (cathode or anode).

The issue of using single potentiostat control of the various current collectors was addressed by Brett et al.,[15] where they adopted the PCB technique introduced by Cleghorn et al.[12] to a single straight channel cathode with each of the current collector ribs on the PCB board being controlled by an individual load. Recently Mench and Wang[16] conducted local current density measurements in direct methanol fuel cells (DMFCs) and hydrogen PEM fuel cells[17] using segmented current collectors, on both the anode and cathode, where the collectors were independently controlled by multichannel potentiostats. Nopenen et al.[18] and Hottinen et al.[19] adopted a similar approach to study steady-state and transient current density distributions in free-breathing PEM fuel cells. In all the above-mentioned studies, MEAs with unsegmented electrodes (the gas diffusion layer and the catalyst layer constitute the electrode) were used. Bender et al.[20] segmented the electrodes along with the current collectors to study local current density distribution in an operating fuel cell. However, Bender et al. applied the segmented assembly only to the anode and not to the cathode.

In a recent publication,[21] the authors of this paper presented results from both modeling and experimental studies comparing the use of MEAs with common and segmented electrodes in current distribution measurements. Significant interaction (current dispersion) or "cross talk " between adjacent segments was detected when an MEA with common electrodes was used in conjunction with a segmented current collector under independent control. The extent of segment-to-segment interactions was found to be dependent on the discharge mode (that is, potentiostatic vs. galvanostatic). The authors concluded that small differences in the contact resistances between the gas diffusion layer (GDL) and the current collectors and the marked anisotropy of the GDL in terms of its conductivity were the primary reasons for such interactions between segments. Current dispersion was eliminated by electronic isolation of the electrodes by segmenting them. The reader is referred to the literature[21] for more details.

The literature reviewed in the previous section mainly addresses the methodology of spatial current density distribution. Only preliminary experimental data are reported in these publications and they are limited to polarization curves (current vs. potential curves) of individual segments generated by holding the segment at a given voltage or current for a few minutes. One of the few exceptions is the work reported by Mench and Wang,[17] in which the authors looked at segment polarization curves generated with step times ranging from a few minutes to an hour. The authors also looked at the effect of step change in the segment potentials on the local current densities over time.

One of the unique features of segmented fuel cell studies is its ability to map over time, the spatial distribution of local current density from initiation of operation until the system reaches steady state. Real-life fuel cell applications are expected to entail such transients in operation such as during startups or step changes in operating conditions such as gas humidity and load. The objective of this work is to evaluate the local current density distribution and its variation over time at different operating conditions at the scale of a single gas channel. It is essential to understand the transient phenomena occurring at this scale to comprehend the bigger picture in terms of single cells and multicell stacks with larger reactive area and multiple gas channels. The type of oxidant used in the cathode, gas stream relative humidity, fuel and oxidant flow rates, and temperature were the operating variables that were addressed in these studies. Given the elaborate matrix of experiments conducted and limitations on the manuscript length, this first part of the series is limited to the experiments addressing the use of pure oxygen as the oxidant and hydrogen-starvation. The second part of this series deals with air operation and temperature case studies.

Experimental

Segmented current collector and flow field

Figure 1a is a schematic of the top view of the current collector and flow field block used in this work. Figure 2 provides the side view of the entire fuel cell assembly. Six rectangular grooves with rounded corners (not shown in the schematic) of precise dimensions of 50 × 15 × 4.85 mm (length × width × depth) were machined into a 180 × 55-mm block of acrylic, using a computer numerically controlled (CNC) milling machine. Bolt holes and pipe threaded gas holes were also machined into the block. Using a CNC milling machine, current-collector strips of dimensions 60 × 15 × 5 mm (length × width × thickness) were machined out of a POCO graphite plate. The graphite plates were then gently pressed into these slots using a precision vice such that the strips extended (10 mm) from one side for electrical connections and quick-setting "super glue " was wicked into the gaps between the grooves and graphite. With a sharp carbide "fly cutter, " the protruding (0.15 mm) graphite surfaces were then machined flat. The graphite strips were placed 7 mm apart. After polishing the surface on fine sandpaper, a single gas channel was machined connecting the inlet and exit hole, as shown in the Figures 1a and 2. The channel was 2 mm in width

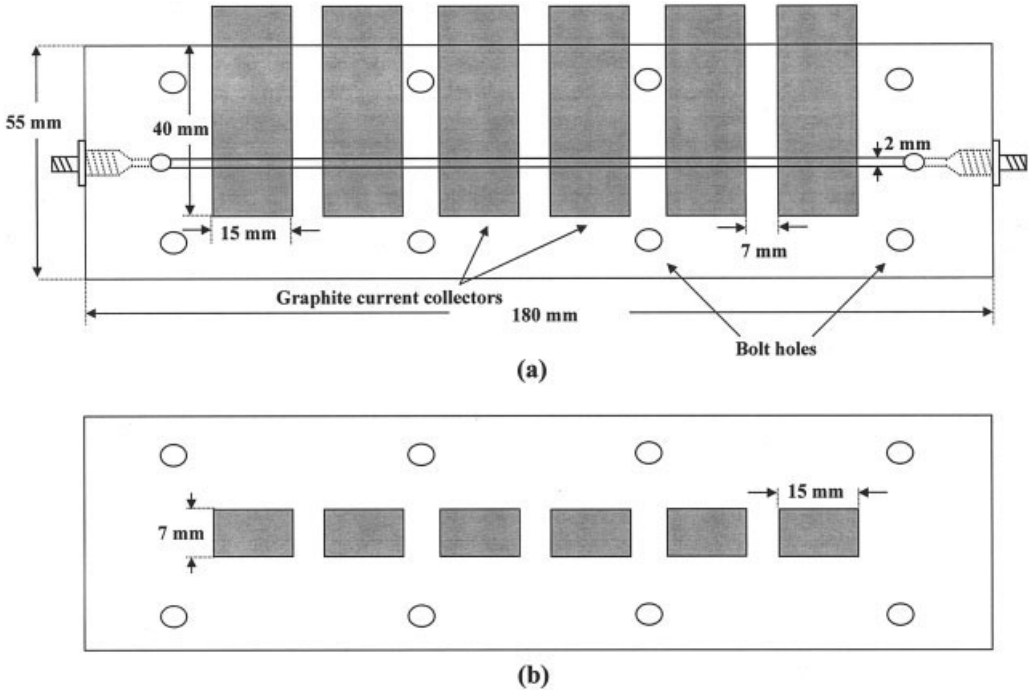

Figure 1. Top view of (a) segmented current collector and flow field block and (b) segmented MEA.

and depth and 125 mm in length (from segment 1 to segment 6). The acrylic block was 25.4 mm thick for the cathode, whereas the anode graphite strips were placed in a 6.25 mm-thick plastic block. A blank 25.4 mm-thick acrylic block was also machined to contain pipe-threaded gas holes and bolt slots along with an aluminum heating block. The heating block had a slot for heating cartridge placement and was insulated on the sides to avoid heat loss and temperature variations along its length. During cell assembly the aluminum heating block was placed on the anode side with O-rings on the gas holes between the blank plate and the thinner acrylic plate containing the graphite strips. Slots were also machined on the back side of the thin acrylic plate and machined copper insets coated with heat compound were placed in these slots. The copper in contact with the aluminum heating block on one side and the graphite strips on the other provided better heat transfer. The

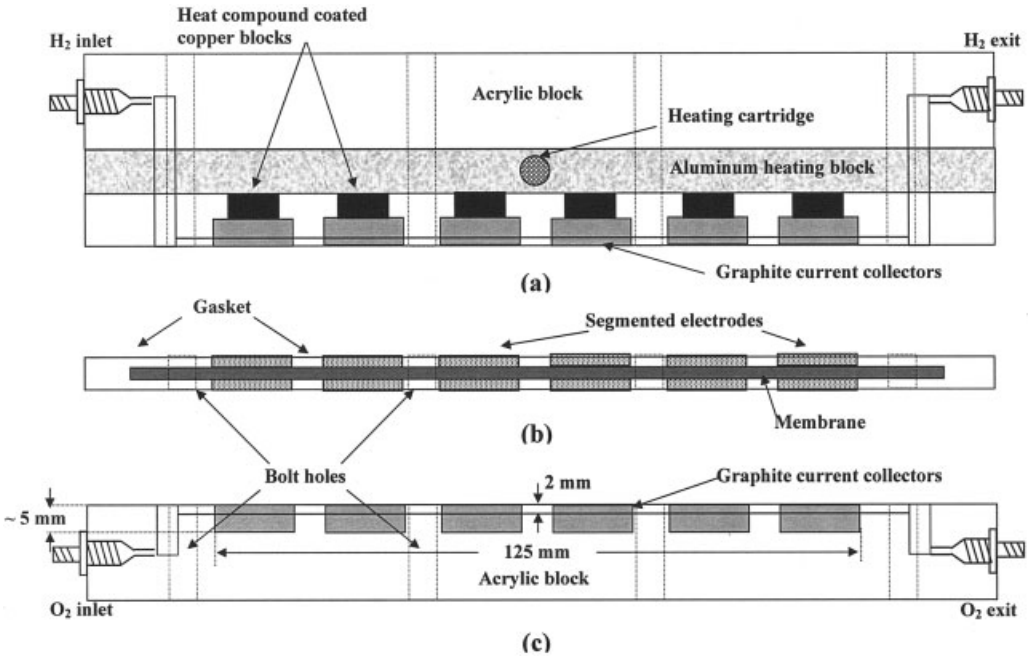

Figure 2. Side view of the segmented fuel cell assembly.

(a) Segmented anode with heating block and acrylic end plate, (b) segmented MEA, and (c) segmented cathode.

Table 1. Summary of Experiments Conducted Indicating Operating Conditions and Objectives

Run	MEA Used	Hydrogen Flow Rate	Hydrogen Humidifier Temperature	Oxygen Flow Rate	Oxygen Humidifier Temperature	Objective
1	MEA 1*	48 cm^3/min ≈ 6.9 A (1.31 A/cm^2)	40°C	19 cm^3/min ≈ 5.5 A (1.05 A/cm^2)	30°C	Test uniformity of segments in MEA 1
2	MEA 1	48 cm^3/min ≈ 6.9 A (1.31 A/cm^2)	Same as above	Same as above	Same as above	Runs 2, 3, and 4 were conducted to study the effect of oxygen flow rate on current density distribution
3	MEA 1	Same as above	Same as above	13.6 cm^3/min ≈ 3.9 A (0.74 A/cm^2)	Same as above	
4	MEA 1	Same as above	Same as above	32.4 cm^3/min ≈ 9.3 A (1.77 A/cm^2)	Same as above	
5	MEA 1	Same as above	50°C	19 cm^3/min ≈ 5.5 A (1.05 A/cm^2)	Same as above	Runs 5 and 6 along with Run 2 were used to study the effect of anode humidifier temperature on current density distribution
6	MEA 1	Same as above	60°C	Same as above	Same as above	
7	MEA 2**	48 cm^3/min ≈ 6.9 A (1.1 A/cm^2)	40°C	19 cm^3/min ≈ 5.5 A (0.87 A/cm^2)	Same as above	Test uniformity of segments in MEA 2
8	MEA 2†	5.1 cm^3/min ≈ 1.47 A (0.28 A/cm^2)	Same as above	19 cm^3/min ≈ 5.5 A (1.05 A/cm^2)	Same as above	Runs 8 and 9 were conducted to look at the effect of hydrogen starvation under dry and humidified conditions
9	MEA 2†	4.5 cm^3/min ≈ 1.3 A (0.25 A/cm^2)	No humidifier	Same as above	No humidifier	

Note: Cell temperature for all runs = 26–28°C.
* Segment 6 in MEA 1 was damaged and was not discharged in Runs 1–6.
**All six segments were in good condition and the flow rates in A/cm^2 are based on active area of six segmented electrodes.
†However, segment 6 was not discharged and used as in in-line OCV sensor in Runs 8 and 9 and flow rates are scaled for five electrodes.

heat compound provided electrical insulation between the common heating block and the individual current collectors. The major planar faces of all the above-mentioned parts of the fuel cell assembly were machine finished and polished and were found to be even within 12.5 μm using a high-precision dial indicator.

MEA fabrication

Electrodes were obtained from TVN Systems, Inc. (Lawrence, KS) that were fabricated by catalyst coating on SIGRACET® GDL 30 BC gas diffusion layers procured from SGL Carbon Composites, Inc. (Gardena, CA). The diffusion layers were 330 μm in thickness. The SIGRACET® diffusion layer had a Teflon® content of 5 wt %. Top and side views of a typical MEA with segmented electrodes on both sides are provided in Figures 1b and 2, respectively. Electrode pieces of dimensions 7 × 15 mm (active area of 1.05 cm^2) were cut from the procured electrode stock. Gaskets were fabricated with slots for the active electrode and holes for bolts to match the segmented flow field/current collector assembly, using precise paper masks with dimensions marked on it using AUTOCAD. Using the gaskets as a frame to accurately arrange the electrodes, the electrodes were hot pressed to Nafion® 112 membranes at 135°C and 65 psi (based on total area including gaskets). Combinations of Teflon® and silicone gaskets were used on both sides of the MEA. Catalyst loadings on both sides were about 0.35 mg Pt/cm^2. As seen in Figure 2, the cathode current collector/flow field was at the bottom, whereas the anode with the heating block was placed on the top. Three MEAs were fabricated for this study to look at the various operating parameters mentioned in the previous section. In all the MEAs used in this study, the anode and cathode had six segments placed laterally along the length of the channel, giving a total reactive area of 6.3 cm^2. However, in the case of MEA 1 segment 6 was damaged during fabrication and all the runs with this MEA involved only five segments corresponding to an active area of 5.25 cm^2. Results from MEA 1 and MEA 2 are presented herein, whereas air operation and temperature studies conducted on MEA 3 are presented in the second part of this series.

Test procedure

Segmented MEAs fabricated as described above were sandwiched between the segmented anode and cathode current collector/flow field assemblies. The bolt holes were used to properly align the electrode and current-collector segments. The cell was assembled in a hydraulic press at the same pressure of 65 psi as the hot-pressing step to avoid any distortion to the MEA arising from excess compression. The cell was tested for gas leak and crossover before data acquisition. The six current collector segments that were in contact with the electrode were each controlled independently using a multichannel potentiostat/galvanostat from Arbin Systems (College Station, TX) through current and voltage leads connected directly to the graphite segments protruding on one side (see Figure 1a). Before the relevant studies addressed in this work, the uniformity in temperature distribution within the cell was also evaluated by measuring the temperature of the various anode and cathode current-collector segments while holding the heating block at 35°C. The average cathode temperature was about 30°C, whereas the anode segments were at 31°C. The variations in temperature from segment to segment on either the cathode or anode was within the accuracy (±1°C) of the T-type thermocouple used showing thermal uniformity at low operating cell temperatures.

Table 1 summarizes the experiments that are discussed herein. All nine experiments were carried out with the heating block held at 30°C. The corresponding average temperature at the cathode was about 26–28°C, with the anode being a couple of degrees higher, depending on ambient conditions. The hot-pressing step involved in the MEA fabrication process leads to dehydration of the Nafion® membrane. Thus, as a first step the

MEAs were subjected to multiple-voltage staircases to massage and rehydrate the membrane and to evaluate the uniformity in the discharge characteristics of the six electrode segments. Runs 1 and 7 represent such massage/evaluation experiments on MEA 1 and MEA 2, respectively. The limits for these potentiostatic staircases were chosen to be 0.8 and 0.65 V with a step size of 50 mV, and the segments were held at each potential for 5 min. The gas flow rates and sparger temperatures are provided in Table 1. The flow rates, staircase limits, and time at each potential step were chosen so as to minimize reactant and water vapor concentration variations along the channel and liquid water accumulation in the electrodes. Once the MEAs were considered to be sufficiently massaged based on reproducibility between cycles, the data from the last potentiostatic cycle were chosen for analyzing the uniformity in discharge characteristics or lack thereof among the various segments. After this massage and uniformity evaluation, Runs 2–6 were conducted on MEA 1 to evaluate the effect of oxygen flow rate (Runs 2, 3, and 4) and hydrogen sparger temperature (Runs 2, 5, and 6). Runs 8 and 9 were conducted on MEA 2 to observe hydrogen starvation while using pure oxygen at the cathode.

During the course of experimentation, it was realized that the history of discharge and thus the water content in the membrane and electrodes affected the subsequent performance of the MEAs. To eliminate this dependency on discharge history, runs pertaining to a specific case study (oxygen flow rate, anode humidification, or fuel starvation) were conducted on subsequent days, and in between each run the MEA was removed from the cell assembly and subjected to an overnight drying process under a lamp and fan.

Studies on MEA 1 (Runs 2–6) addressing oxygen stoichiometric flow rates and anode humidification were conducted as follows. After the overnight drying process, the MEA was assembled as mentioned above and electrode segments (MEA 1 had only five working segments) were subjected to a liquid water "load-up " step, wherein each electrode was simultaneously discharged at a constant current of 100 mA for 1 h. This step was included in the experimental scheme to rehydrate the MEA that was dried overnight. Hydrogen and oxygen flow rates and sparger temperatures used in this load-up step were the same as in the massage experiments. The galvanostatic "load-up " step that specified the water generation rate (by specifying the reaction rate) was expected to ensure uniformity in the water accumulation in each electrode. After the constant current step, the gas flow rates and sparger temperatures were adjusted to the desired values preselected for the study and the segments were held at a constant voltage of 0.6 V for 2 h and the current response was recorded overtime. Care was taken to initiate this step after ensuring that the sparger temperatures and gas flow rates stabilized at the desired values.

For hydrogen-starvation studies on MEA 2, all six segments were subjected to a "load-up " step that lasted 30 min. After "load-up " the desired flow rate and sparger temperatures were established and the first five segments from the inlet were subjected to three sequential potential steps of 0.7, 0.6, and 0.55 V. The segments were held at each potential for 30 min. Segment 6 was not discharged during this potentiostatic sequence and was used as an in-line open circuit voltage (OCV) sensor.

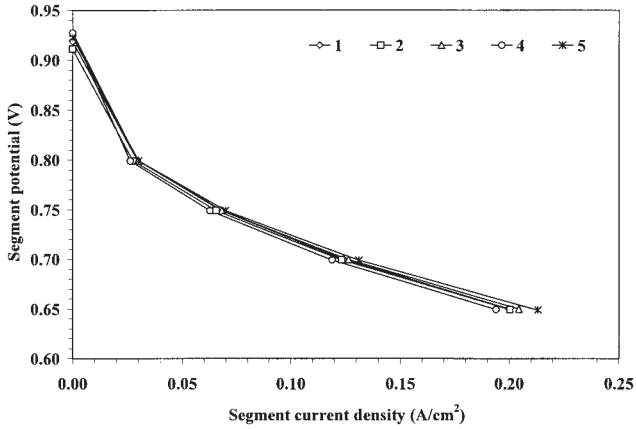

Figure 3. Polarization curves from Run 1 for segments in MEA 1.

H_2 flow rate = 48 cm^3/min (6.9 A or 1.31 A/cm^2); O_2 flow rate = 19 cm^3/min (5.5 A or 1.05 A/cm^2); H_2 humidifier temperature = 40°C; O_2 humidifier temperature = 30°C; and cell temperature = 27–28°C.

Results and Discussion

Effect of oxygen flow rate

The current responses of the five segments in MEA 1 from the last potentiostatic staircase of Run 1 are provided in Figure 3 in the form of polarization curves. These curves show that the segment performances under the chosen experimental conditions were reasonably uniform. Segment 5 consistently performed the best, whereas segment 4 showed the poorest performance. At 0.65 V the current responses of the segments were within 25 mA/cm^2 of each other (0.195–0.22 mA/cm^2). Based on the use of pure hydrogen and oxygen streams that were reasonably humidified for a cell temperature of 26–28°C, this difference in segment performance may be attributed to inherent variations in the GDL and catalyst layer properties. The uniformity achieved with this MEA was deemed satisfactory for oxygen flow rate and hydrogen humidification studies.

Figure 4 corresponds to Run 2 and provides the current response over 2 h of five segments that were held at 0.6 V with an oxygen flow rate of 19 cm^3/min equivalent to 5.5 A (1.05 A/cm^2 based on a total area of 5.25 cm^2; 1.05 cm^2 per electrode). Other relevant details are available in Table 1. The initial local current density distribution along the channel matches well with the results obtained in Run 1 (see Figure 3). Segment 5 provides the maximum current density around 0.375 A/cm^2, whereas segment 4 is the lowest at 0.33 A/cm^2. The other three segments lie within this range. However, as time progresses, the current density at segment 5 starts to drop quickly and finally settles at a limiting current of about 0.03 A/cm^2 after about 40 min of discharge. The other segments held steady at their initial values over the entire course of the experiment.

Based on the operating conditions used in this run, the decrease in current density at segment 5 can be attributed solely to liquid water flooding. The use of pure oxygen at sufficiently high flow rates eliminated any oxygen concentration effects along the channel length. A brief analysis of the liquid water transport processes involved in the cathode of a PEM fuel cell using conventional gas distributors[8] is necessary at this junc-

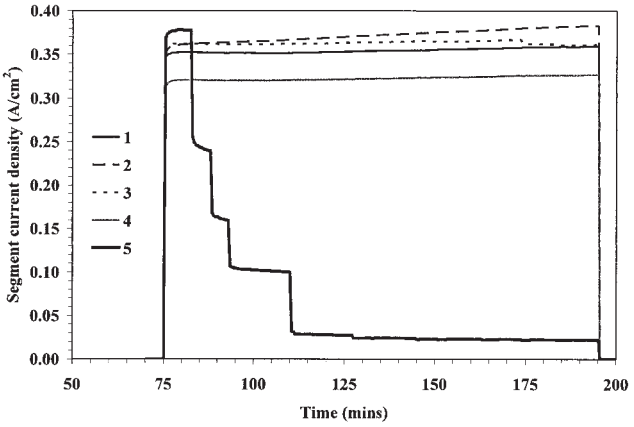

Figure 4. Individual segment current response to an imposed voltage of 0.6 V obtained from Run 2 (segment potentials controlled independently).

H_2 flow rate = 48 cm^3/min (6.9 A or 1.31 A/cm^2); O_2 flow rate = 19 cm^3/min (5.5 A or 1.05 A/cm^2); H_2 humidifier temperature = 40°C; O_2 humidifier temperature = 30°C; and cell temperature = 27–28°C.

ture to explain the results observed. At any given potential, the current density achieved is a strong function of the water saturation within the cathode. The two sources for liquid water in the cathode are electro-osmotic drag of the protons traversing across the membrane from the anode to the cathode and generation by the electrochemical reaction. The liquid water is removed from the cathode by three mechanisms: back-diffusion across the membrane from the cathode to anode, evaporation and diffusion of water vapor, and liquid water transport. Liquid water is transported solely by a capillary mechanism within the diffusion layer and upon reaching the channel–GDL interface it is transported along the length of the channel by the drag force exerted on the liquid arising from the convective flow of gas in the channel. Because evaporation and water vapor transport are relatively faster than liquid water transport, liquid water will be observed in the channel only after the gas stream has been completely saturated with water vapor. Beyond this point of complete gas saturation with water vapor, liquid water appears in the channel and the rates of its transport and distribution in the channel depend on the gas velocity and the wettability of the channel material. The presence of liquid water in the channel can reduce the rate of wicking from the electrodes downstream because the channel–diffusion layer interface is no longer dry and this reduces the water saturation gradient in the electrodes downstream, thereby reducing the rate of water transport by capillary action. Moreover, it is intuitively evident that while using conventional flow fields, once electrodes are flooded, the only mechanism available for clearing the flooded electrodes is evaporation, achieved by increasing either the temperature or the gas flow rate.

Evidence is available in the literature that spargers are not very efficient and the gas stream is never more than 60% saturated at a given sparger temperature.[20] Thus in run 2, despite the cathode sparger and the cell being at the same temperature, the oxygen stream was not fully saturated. Thus segments closer to the inlet saw relatively drier oxygen that helped liquid water removal by evaporation. Further downstream the oxygen gas stream became saturated, resulting in the presence of liquid water in the channel. Probably, the amount of liquid water in the channel also increased along the length of the channel beyond the point of gas saturation. Based on this discussion we believe that significant accumulation of liquid water occurred in the channel in the vicinity of segment 5, leading to serious liquid water flooding within the electrode. In other words, the chosen operating conditions provided a net water removal capacity that could accommodate only the generation rates equivalent to the first four segments. The 40 min over which segment 5 flooded, causing a drop in current density to limiting values, represent the time associated with liquid water filling up the pore volume in electrode 5. This time period is expected to be a function of the net difference in the water generation and removal rates. It is also seen from Figure 4 that near steady state, a peak in local current density distribution along the channel is observed at segment 2, suggesting mild dehydration at segment 1.

As mentioned earlier, liquid water movement in the channel is a strong function of gas velocity. When unsaturated, gas flow rates also dictate the evaporation capacity. To verify the above-mentioned inferences, Runs 3 and 4 were conducted with lower and higher oxygen flow rates, whereas other operating conditions were maintained similar to those in Run 2. Figure 5 provides the current density distribution along the channel over time obtained from Run 3 when a lower oxygen flow rate of 13.6 cm^3/min (3.9 A; 0.74 A/cm^2) was used. By lowering the oxygen flow rate, the evaporation capacity and liquid water removal by drag were reduced, resulting in the gas stream becoming saturated more rapidly and closer to the inlet. Figure 5 supports this argument wherein segment 5 floods more rapidly in comparison to Run 2 and reaches the same limiting current density of about 0.03 mA/cm^2 within 20–25 min. Also, segments 3 and 4 start to exhibit a significant decrease in current densities over the course of the experiment, suggesting the presence of liquid water closer to the inlet than in Run 2. Thus, as expected, the number of segments that are not flooded is determined by the difference in the water generation to

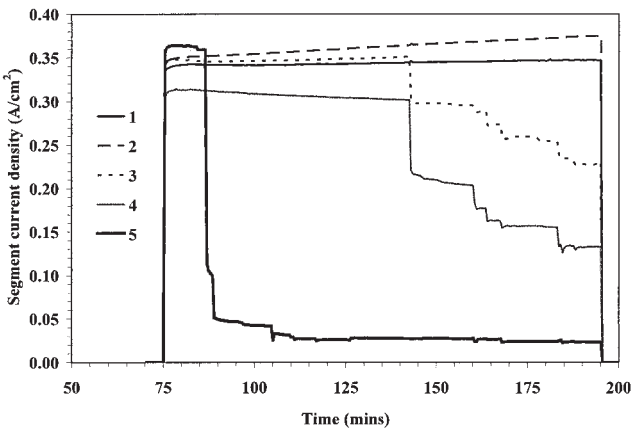

Figure 5. Individual segment current response to an imposed voltage of 0.6 V obtained from Run 3 (segment potentials controlled independently).

H_2 flow rate = 48 cm^3/min (6.9 A or 1.31 A/cm^2); O_2 flow rate = 13.6 cm^3/min (3.9 A or 0.74 A/cm^2); H_2 humidifier temperature = 40°C; O_2 humidifier temperature = 30°C; and cell temperature = 27–28°C.

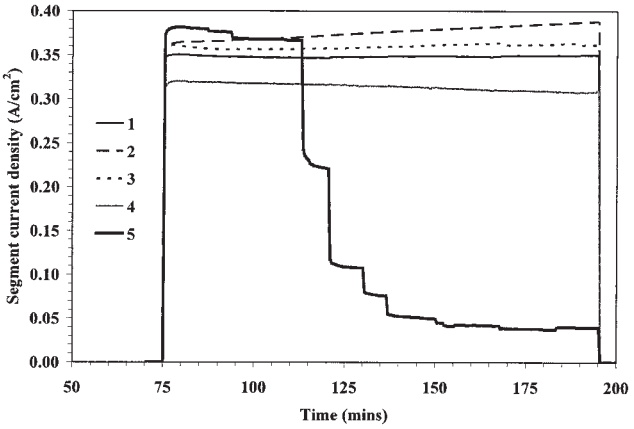

Figure 6. Individual segment current response to an imposed voltage of 0.6 V obtained from Run 4 (segment potentials controlled independently).

H_2 flow rate = 48 cm^3/min (6.9 A or 1.31 A/cm^2); O_2 flow rate = 32.4 cm^3/min (9.3 A or 1.77 A/cm^2); H_2 humidifier temperature = 40°C; O_2 humidifier temperature = 30°C; and cell temperature = 27–28°C.

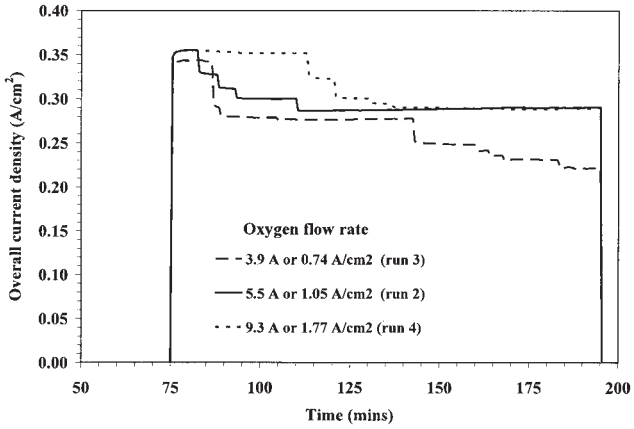

Figure 7. Effect of oxygen flow rate on the average cell current density with individual segment potentials controlled independently at 0.6 V (Runs 2, 3, and 4).

H_2 flow rate = 48 cm^3/min (6.9 A or 1.31 A/cm^2); H_2 humidifier temperature = 40°C; O_2 humidifier temperature = 30°C; and cell temperature = 27–28°C.

removal rates. Here again the initial current responses are quite consistent with the results from previous runs (1 and 2).

Results from Run 4 are provided in Figure 6, where oxygen was supplied at a higher flow rate of 32.4 cm^3/min (9.3 A; 1.77 A/cm^2). As expected, by increasing the oxygen flow rate, the water removal by drag in the channel and by evaporation was improved. This resulted in delaying the onset of flooding in segment 5 to almost 1 h. However, even at this flow rate, the water removal rate was not sufficient for segment 5, resulting in an eventual drop in the current density to a limiting value close to 0.03 mA/cm^2. The difference in performance of segments 1 and 2 is also greater in this run, indicating a higher dehydration effect at the inlet than in Run 2 because of the higher flow rate. Finally, the results from Runs 2, 3, and 4 are also provided as average current density of the entire fuel cell in Figure 7. As seen in this figure, by increasing the oxygen flow rate, the net accumulation rate of water in the electrode is reduced, thereby improving performance. Detailed information such as fractional reactive area utilization, point of gas saturation, and severity of flooding along the channel is lost when experiments are conducted using unsegmented fuel cells that yield data such as in Figure 7 and only an overall inference that higher flow rates reduces liquid water flooding in the electrodes can be drawn.

Effect of anode sparger temperature

As mentioned before, another major player in water removal from the cathode is back-diffusion of water across the membrane to the anode. This diffusion rate is expected to be influenced by the humidification level of the anode gas stream. In Runs 5 and 6 higher anode sparger temperatures were used to evaluate the effect of the humidity level of the fuel stream on the local current density distribution along the channel.

Figures 8 and 9 provide the current responses of the segmented fuel cell when the anode sparger was maintained at 50 and 60°C, respectively, while maintaining other pertinent operating conditions constant. On comparing Figures 4 and 8, it is clear that increasing the anode sparger temperature from 40 to 50°C did not have a significant impact on the current density distribution along the length of the channel. Current density at segment 5 dropped to about the same limiting value after 40 min of discharge as in Run 2. Segments 1, 2, and 3 show similar performance in Runs 2 and 5. Figure 8 also indicates a minor drop in the performance of segment 4 that was not observed in Run 2, where the sparger was at a lower temperature.

On the other hand, a further increase in the sparger temperature to 60°C significantly affected the local current density distribution over the course of discharge as seen in Figure 9 representing Run 6. Although the behavior of segment 5 is comparable to that of previous runs, segments 3 and 4 also showed a decrease in current densities about 35 min into

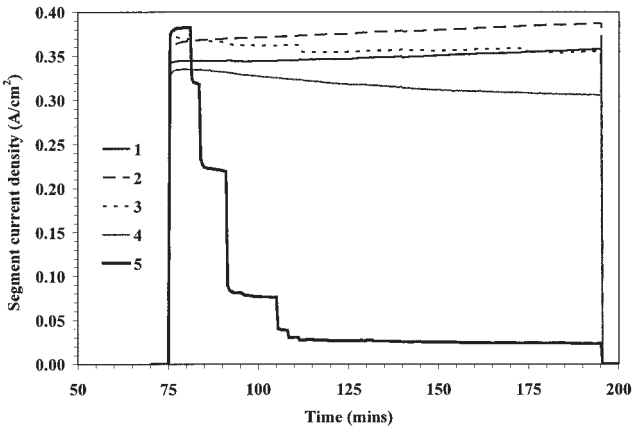

Figure 8. Individual segment current response from Run 5 at an imposed voltage of 0.6 V (segment potentials controlled independently).

H_2 flow rate = 48 cm^3/min (6.9 A or 1.31 A/cm^2); O_2 flow rate = 19 cm^3/min (5.5 A or 1.05 A/cm^2); H_2 humidifier temperature = 50°C; O_2 humidifier temperature = 30°C; and cell temperature = 27–28°C.

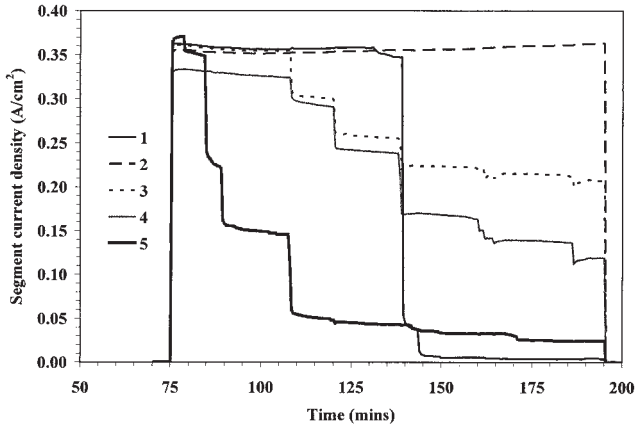

Figure 9. Individual segment current response from Run 6 at an imposed voltage of 0.6 V (segment potentials controlled independently).

H_2 flow rate 48 cm^3/min (6.9 A or 1.31 A/cm^2); O_2 flow rate = 19 cm^3/min (5.5 A or 1.05 A/cm^2); H_2 humidifier temperature = 60°C; O_2 humidifier temperature = 30°C; and cell temperature = 27–28°C.

discharge. Moreover, around 70 min after the initiation of the experiment, current density at segment 1 dramatically dropped to limiting values in the range of 0.005 A/cm^2.

By increasing the inlet stream humidity at the anode, the net amount of liquid water removed from the cathode by back-diffusion was reduced as a result not only of the decrease in the saturation gradient across the membrane that is the driving force but also of the increased electro-osmotic drag exhibited by better hydrated membranes. This reduction in one of the major mechanisms of water removal resulted in the oxygen stream becoming saturated significantly earlier, leading to the appearance of water in the cathode gas channel closer to the inlet, causing segments 3 and 4 to decline in performance. The current density drop at segment 1 is believed to be an experimental artifact induced by the orientation of the segmented fuel cell assembly. Because of the 30°C difference between the anode sparger and the cell temperature, significant condensation occurred at the pipe-threaded fittings and machined feeder holes in the blank acrylic and aluminum blocks. When this volume was filled, a bead of water was transported into the anode gas channel by the hydrogen stream. Because the electrode on the anode side was placed below the channel, this bead completely soaked the first anode segment, thereby quenching the current at segment 1. Visual observation of MEA 1 after Run 6 showed that the anode on the first segment was completely saturated with water, thus supporting the above theory. Figure 10 provides the results of Runs 2, 5, and 6 summarized as average current densities of the entire cell over time. The water vapor saturation pressures at 40, 50, and 60°C are 0.073, 0.095, and 0.122 atm, respectively. This nonlinear temperature dependency is the probable reason for the lack of significant differences between Runs 2 and 5 in comparison with the dramatic effects in Run 6.

A major observation that must be addressed before closing the discussion on the effect of oxygen flow rates and anode humidification is the actual nature of the flooding phenomenon. In all the results analyzed so far, the flooding behavior is characterized by a sharp discrete stepwise drop in the local current densities. It is our belief that these discrete flooding steps are closely related to the pore size distribution within the electrode. It is well known that the relationship between the capillary pressure and liquid water saturation is a strong function of pore sizes and wettability. We hypothesize that stepwise drops in the current density represent the filling up of pores of different pore radii and Teflon® content. Once the liquid water fills up the majority of the pores in an electrode, the continuity of the gas phase within the electrode is severely compromised and the sustainable current density will be in the order of a few tens of milliamperes/cm^2 as the limiting currents observed in these experiments.

Effect of fuel starvation

To achieve higher overall efficiency and reduce parasitic losses associated with recycling equipments, fuel cells are usually operated with fuel supply that is only slightly greater than the reaction demand (usually 1.1–1.3 × stoichiometric rate). Depending on changes in operating conditions, such as load and temperature, this can lead to temporary fuel starvation. The change in the spatial distribution of local current densities over time when the fuel cell is subjected to hydrogen starvation is of interest and is the focus of the experiments discussed in this section. Fuel starvation is known to degrade the catalyst microstructure because of excessive heat generation and possible support oxidation.[22] Thus a separate MEA (MEA 2) was assigned for these experiments. Also, only a couple of experiments were conducted on MEA 2 to avoid the results from being affected by local catalyst layer microstructure modification. In these experiments the hydrogen exit was routed through long vertical tubing with one end placed in a water reservoir. Under hydrogen-starvation conditions, the pressure near the exit of the anode channel dropped below atmospheric and the water in the reservoir rose in the tubing to accommodate this drop. This procedure prevented ambient air from being sucked into the anode chamber.

Run 7 was conducted to massage MEA 2 and to analyze the

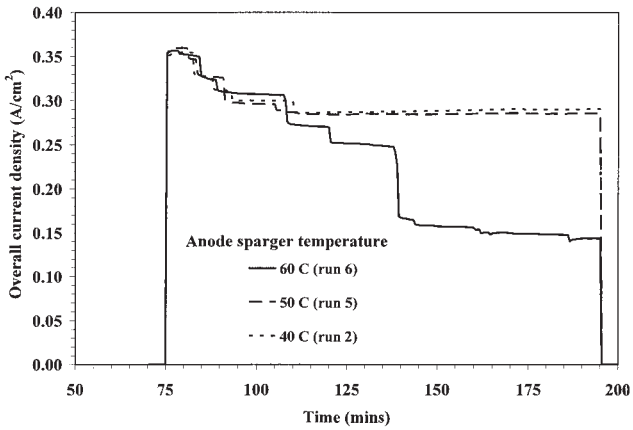

Figure 10. Effect of anode humidifier temperature on the average cell current density with individual segment potentials controlled independently at 0.6 V (Runs 2, 5, and 6).

H_2 flow rate = 48 cm^3/min (6.9 A or 1.31 A/cm^2); O_2 flow rate = 19 cm^3/min (5.5 A or 1.05 A/cm^2); O_2 humidifier temperature = 30°C; and cell temperature = 27–28°C.

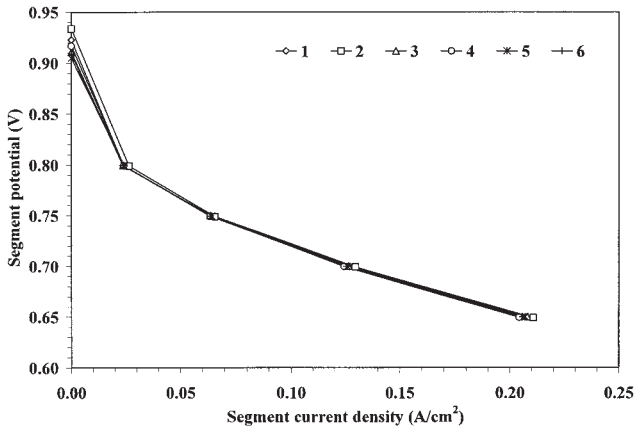

Figure 11. Polarization curves for segments in MEA 2 from Run 7.

H_2 flow rate = 48 cm^3/min (6.9 A or 1.1 A/cm^2); O_2 flow rate = 19 cm^3/min (5.5 A or 0.87 A/cm^2); H_2 humidifier temperature = 40°C; O_2 humidifier temperature = 30°C; and cell temperature = 27–28°C. (Note: Flow rates scaled to six segments.)

uniformity among the electrode segments in terms of its current–voltage response. The current responses to the final voltage staircase of this massage experiment are provided in Figure 11. In comparison to Figure 3, which shows the results from a similar experiment (Run 1) on MEA 1, it is quite evident that much better uniformity in performance was achieved in MEA 2. For instance, the current densities at the six segments were within 10 mA at 0.65 V, whereas the spread in MEA 1 was about 25 mA. The large electrode pieces procured from TVN Systems, Inc. usually showed signs of catalyst ink seepage into the GDL at the edges. Unlike MEA 1, these edges were avoided in the electrode pieces that were cut out for MEA 2, which we think is the reason for the better uniformity in performance.

Runs 8 and 9 were conducted on MEA 2, in which five out of the six segments were subjected to a three-step potentiostatic discharge as explained in the previous sections. Segment 6 was used as an in-line voltage sensor. The relevant experimental conditions are provided in Table 1. Run 8 was conducted with humidified gas streams, whereas neither of the gas streams was humidified in Run 9. Hydrogen flow rates of 5.1 cm^3/min (1.47 A) and 4.5 cm^3/min (1.3 A) were used in Runs 8 and 9, respectively. The same exact flow rates could not be achieved for these two runs because of the lack of precision of the metering valve/rotameter setup at this flow rate range.

Figure 12 provides the current responses from Run 8 for the three voltage steps. When the segments were held at 0.7 V, the hydrogen supply was in excess of the reaction demand. Moreover, the gas streams were sufficiently humidified. Thus the local current densities were uniform (within 5 mA) along the channel length, as shown in the inset. Once the reaction driving force was increased by decreasing the segment potentials to 0.6 V, starvation effects were observed. More than 70% of the hydrogen supplied was consumed by the first three segments at an average of 0.36 A/cm^2 per segment. This resulted in lack of sufficient fuel for segments downstream, as indicated by a decline in performance of segments 4 and 5. Segment 5, which is the furthest from the inlet, was the most affected with current densities in the range of 0.015 A/cm^2, whereas segment 4 discharged at about 0.275 A/cm^2. Upon a further decrease in

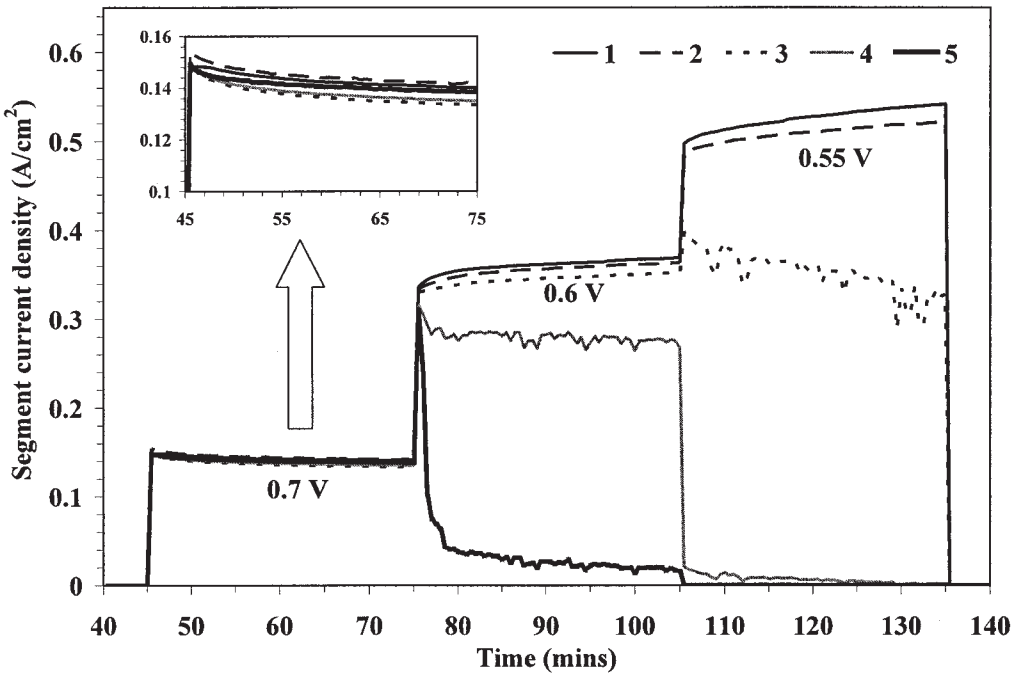

Figure 12. Individual segment current response from Run 8 at various applied segment potentials under fuel-starvation conditions.

Inset provides an enlargement at 0.7 V. H_2 flow rate = 5.1 cm^3/min (1.47 A or 0.28 A/cm^2); O_2 flow rate = 19 cm^3/min (5.5 A or 1.05 A/cm^2); H_2 humidifier temperature = 40°C; O_2 humidifier temperature = 30°C; and cell temperature = 27–28°C.

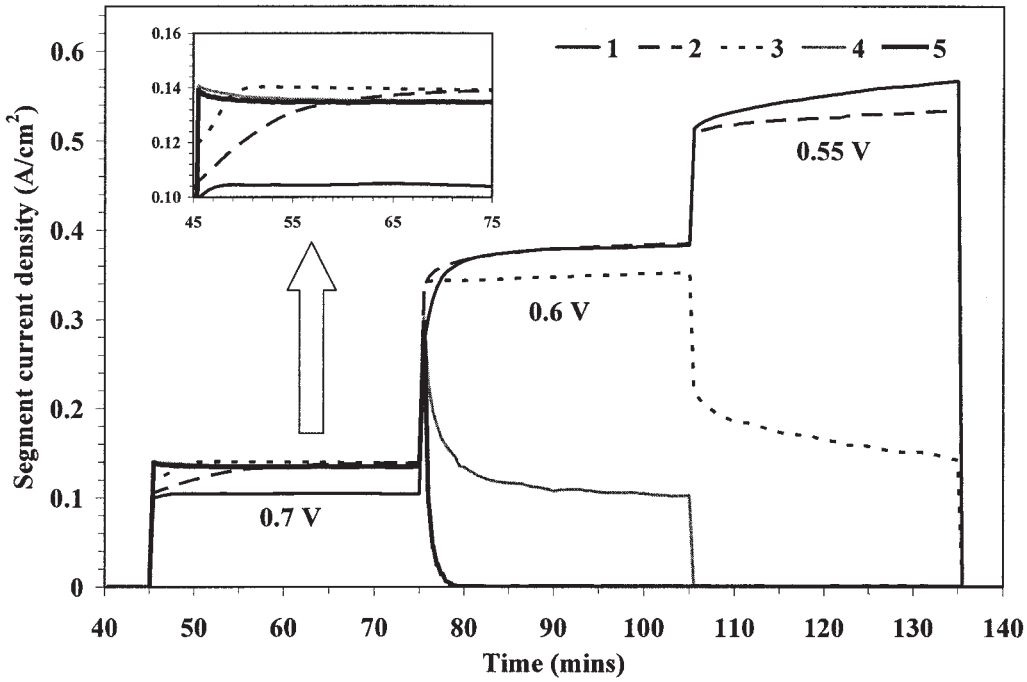

Figure 13. Individual segment current response from Run 9 at various applied segment potentials under fuel-starvation conditions.

Inset provides an enlargement at 0.7 V. H_2 flow rate = 4.5 cm^3/min (1.3 A or 0.25 A/cm^2); O_2 flow rate = 19 cm^3/min (5.5 A or 1.05 A/cm^2); dry H_2 and O_2; and cell temperature = 27–28°C.

the operating potential, most of the hydrogen was consumed at segments 1 and 2. This resulted in starvation effects being observed as close to the inlet as segment 3. Segments 4 and 5 were completely deprived of fuel and their current responses were close to zero.

Figure 13 provides the results from Run 9, which were similar in all aspects to Run 8 expect for the lack of humidification (and slightly lower hydrogen flow rate). In this case, at a segment potential of 0.7 V, fuel flow rates were sufficiently higher than reaction demand and the current density distribution along the channel was dominated by membrane dehydration (see enlarged inset). Segment 1, which is closest to the inlet, was subjected to completely dry gases and showed the lowest current density. Along the length of the channel, the gases were humidified over time by the product water generated at the cathode. This is clearly seen from the current responses of segments 2 and 3 that started out quite low (close to segment 1) and improved over time. Segments 5 and 6 benefited from humidification by product water from the very beginning of the experiment. The dehydration pattern of the membrane provided a current spread of about 40 mA. Once the segment potentials decreased to 0.6 V, a transition was observed in the current density distribution from being dependent on membrane hydration to fuel availability. Because of the higher rate of water generation by reaction, segment 1 and, to a certain extent, segment 2 were quickly humidified within a few minutes and their current performances were the maximum as a result of greater fuel availability. The effect of hydrogen starvation was exhibited by segments 4 and 5 (segment 3 showed some minor effects). The effect on segment 4 was greater in this run than in Run 8 because of the slightly lower hydrogen flow rates. A further increase in the reaction driving force resulted in complete fuel depletion at segments 4 and 5, causing the current density to drop to zero. Segment 3 also showed a significant starvation effect that was greater in this run than that in Run 8 because of the lower fuel flow rate. The average current density of all five segments is provided in Figure 14 for Runs 8 and 9. At 0.7 V, when fuel is available in excess, the overall cell performance is dominated by dehydration effects. Run 9, in which the gases were not humidified, showed lower overall current densities, reflecting the losses at the segments closer to the inlet. At lower segment potentials, as expected, fuel availability dictated the overall current densities. Figure 14 indicates nearly complete consumption of fuel beyond 0.6 V.

The potential measured at segment 6 for the above two runs are plotted in Figure 15. At high segment potentials, when fuel was in excess, segment 6 registered typical open circuit voltage values close to 1.0 V. As the fuel cell was taken to starvation regimes, the potential at segment 6 reflected the complete consumption of fuel. The voltage signal is also a result of some air crossover to the anode side as a result of the pressure difference caused by starvation. In Run 9, at 0.6 V (hydrogen flow rate = 4.5 cm^3/min) nearly complete consumption of hydrogen occurred near segment 4 and current density at segment 5 was close to zero. The voltage signal from segment 6 matches well with the current responses, indicating minimal availability of hydrogen past segment 5. On the contrary, in Run 8 with a higher fuel flow rate (5.1 cm^3/min) current density at segment 5 goes to zero only after about 20 min into the 0.55-V potential step that is also captured in the voltage response of segment 6. There seems to be a lag between the

current response of segment 5 and the voltage response of segment 6, which can be attributed to the time for consumption of hydrogen available in the pore spaces of the electrode and the channel. Also, before starvation the voltage signal at segment 6 increases when the current density and thus water generation is increased at preceding segments, indicating improvement in the hydration of membrane region at segment 6.

Conclusions

A segmented electrode/current collector fuel cell assembly was used to examine the effect of oxygen flow rate, anode sparger temperature, and hydrogen starvation on the spatial and temporal distribution of local current densities along a single gas channel.

The local current density distribution along the channel was studied for more than 2 h at three different oxygen flow rates of 13.6, 19, and 36.4 cm^3/min corresponding to 0.74, 1.05, and 1.77 A/cm^2. The lowest flow rate resulted in partial flooding in segments 3 and 4, whereas segment 5 was completely flooded within 20 min of discharge. Flooding at segments 3 and 4 was avoided at higher oxygen flow rates. Higher flow rates also delayed the onset of flooding at segment 5.

Increasing the anode sparger temperature from 40 to 50°C did not significantly change the local current density distribution. A further increase in the sparger temperature to 60°C resulted in loss in performance at segments 3 and 4 as a result of the net reduction in the water removal rate from the cathode by back diffusion. The orientation of the assembly combined with condensation in inlet gas fittings at the anode caused flooding at the anode of segment 1.

When fuel supply was plentiful, the local current distribution was determined by the hydration state of the membrane. Humidified gas streams that helped membrane hydration provided uniformity in the current densities along the channel. The use of dry gases resulted in a substantial loss in the performance of segments that were closer to the inlet. Under fuel-starvation conditions, the segments furthest from the inlet were the most affected. The segments closer to the inlet dominated the overall

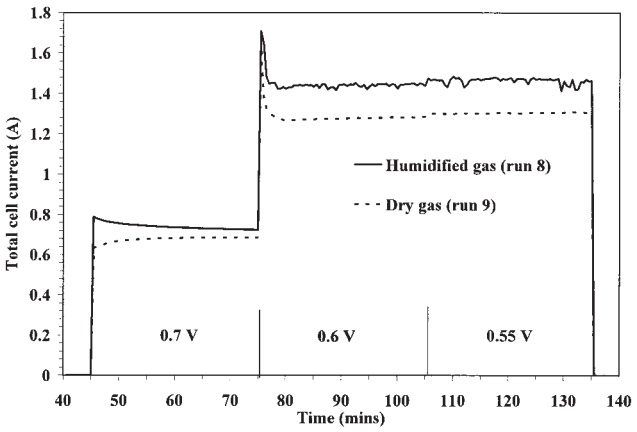

Figure 14. Effect of dry inlet gas steams vs. humidified gas streams in terms of overall current from the cell (Runs 8 and 9).

H_2 flow rate = 5.1 or 4.5 cm^3/min (1.47 or 1.3 A); O_2 flow rate = 19 cm^3/min (5.5 A or 1.05 A/cm^2); and cell temperature = 27–28°C.

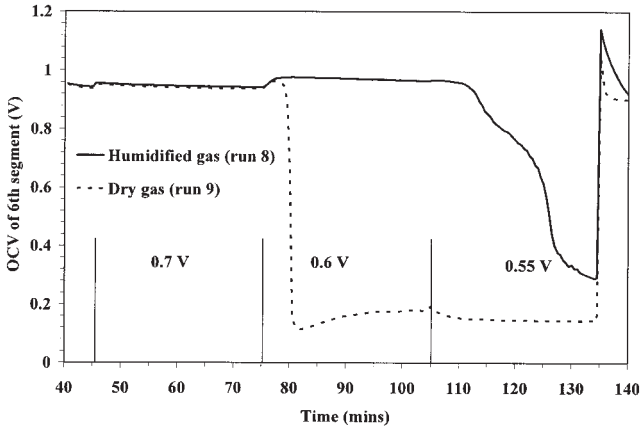

Figure 15. Sixth segment open circuit potential response during Runs 8 and 9.

H_2 flow rate = 5.1 or 4.5 cm^3/min (1.47 or 1.3 A); O_2 flow rate = 19 cm^3/min (5.5 A or 1.05 A/cm^2); and cell temperature = 27–28°C.

cell performance at lower operating voltages, whereas current generation at downstream segments was negligible. A novel technique involving the use of one of the electrode segments as an in-line voltage sensor that indicates availability of reactants was also demonstrated.

The same setup was also used to study the local current density distribution under air operation and the effect of higher cell temperatures. The results from these experiments are discussed in the second part of this series.

Acknowledgments

This work was supported by the National Science Foundation under Grant CTS-9910923.

Literature Cited

1. Springer TE, Wilson MS, Gottesfeld S. Modeling and experimental diagnostics in polymer electrolyte fuel cells. *J Electrochem Soc*. 1993; 140:3513-3526.
2. Bernardi DM, Verbrugge MW. A mathematical model of the solid-polymer-electrolyte fuel cell. *J Electrochem Soc*. 1992;139:2477-2491.
3. Nguyen TV, White RE. A water and heat management model for proton-exchange-membrane fuel cells. *J Electrochem Soc*. 1993;140: 2178-2186.
4. West AC, Fuller TF. Influence of rib spacing in proton-exchange membrane electrode assemblies. *J Appl Electrochem*. 1996;26:557-565.
5. Gurau V, Liu H, Kakac S. Two-dimensional model for proton exchange membrane fuel cells. *AIChE J*. 1998;44:2410-2422.
6. Shimpalee S, Dutta S. Numerical prediction of temperature distribution in PEM fuel cells. *J Numer Heat Transfer*. 2000;38:111-128.
7. Natarajan D, Nguyen TV. A two-dimensional, two-phase, multi-component, transient model for the cathode of a proton exchange membrane fuel cell using conventional gas distributors. *J Electrochem Soc*. 2001;148:1324-1335.
8. Natarajan D, Nguyen TV. Three-dimensional effects of liquid water flooding in the cathode of a PEM fuel cell. *J Power Sources*. 2003; 115:66-80.
9. Yi JS, Nguyen TV. An along-the-channel model for proton exchange membrane fuel cells. *J Electrochem Soc*. 1998;145:1149-1159.
10. He W, Yi JS, Nguyen TV. Two-phase flow model of the cathode of PEM fuel cells using interdigitated flow fields. *AIChE J*. 2000;46: 2053-2064.
11. Wang ZH, Wang CY, Chen KS. Two-phase flow and transport in the

air cathode of proton exchange membrane fuel cells. *J Power Sources*. 2001;94:40-50.
12. Cleghorn SJC, Derouin CR, Wilson MS, Gottesfeld S. A printed circuit board approach to measuring current distribution in a fuel cell. *J Appl Electrochem*. 1998;28:663-672.
13. Stumper J, Campbell SA, Wilkinson DP, Johnson MC, Davis M. In-situ methods for the determination of current distribution in PEM fuel cells. *Electochim Acta*. 1998;43:3773-3783.
14. Wieser Ch, Helmbold A, Gulzow E. A new technique for two-dimensional current distribution measurements in electrochemical cells. *J Appl Electrochem.* 2000;30:803-807.
15. Brett DJL, Atkins S, Brandon NP, Vesovic V, Vasileiadis N, Kucernak AR. Measurement of the current distribution along a single flow channel of a solid polymer fuel cell. *Electrochem Commun*. 2001;3: 628-632.
16. Mench MM, Wang CY. An *in situ* method for determination of current distribution in PEM fuel cells applied to a direct methanol fuel cell. *J Electrochem Soc*. 2003;150:A79-A85.
17. Mench MM, Wang CY. *In situ* current distribution measurements in polymer electrolyte fuel cells. *J Electrochem Soc*. 2003;150:A1052-A1059.
18. Nopenen M, Mennola T, Mikkola M, Hottinen T, Lund P. Measurement of current distribution in a free-breathing PEMFC. *J Power Sources*. 2002;106:304-312.
19. Hottinen T, Nopenen M, Mennola T, Himanen O, Mikkola M, Lund P. Effect of ambient conditions on performance and current distribution of a polymer electrolyte membrane fuel cell. *J Appl Electrochem*. 2003;33:265-271.
20. Bender G, Wilson MS, Zawodzinski TA. Further refinements in the segmented cell approach to diagnosing performance in polymer electrolyte fuel cells. *J Power Sources*. 2003;123:163-171.
21. Natarajan D, Nguyen TV. Effect of electrode configuration and electronic conductivity on current density distribution measurements in PEM fuel cells. *J Power Sources*. 2004;135:95-109.
22. Taniguchi A, Akita T, Yasuda K, Miyazaki Y. Analysis of electrocatalyst degradation in PEMFC caused by cell reversal during fuel starvation. *J Power Sources*. 2004;130:42-49.

Manuscript received Jun. 9, 2004, and revision received Feb. 2, 2005.